A three-dimensional modelling of the layered structure of comet 67P/Churyumov-Gerasimenko

Luca Penasa, Matteo Massironi, Giampiero Naletto, Emanuele Simioni, Sabrina Ferrari, Maurizio Pajola, Alice Lucchetti, Frank Preusker, Frank Scholten, Laurent Jorda, et al.

Monthly Notices
of the
ROYAL ASTRONOMICAL SOCIETY

MNRAS **469,** S741–S754 (2017)
Advance Access publication 2017 November 13

doi:10.1093/mnras/stx2899

A three-dimensional modelling of the layered structure of comet 67P/Churyumov–Gerasimenko

L. Penasa,[1⋆] M. Massironi,[1,2⋆] G. Naletto,[1,3,4] E. Simioni,[4,5] S. Ferrari,[1] M. Pajola,[6] A. Lucchetti,[5] F. Preusker,[7] F. Scholten,[7] L. Jorda,[8] R. Gaskell,[9] F. Ferri,[1] F. Marzari,[10] B. Davidsson,[11] S. Mottola,[7] H. Sierks,[12] C. Barbieri,[1,10] P. L. Lamy,[13] R. Rodrigo,[14,15] D. Koschny,[16] H. Rickman,[17,18] H. U. Keller,[7,19] J. Agarwal,[12] M. F. A'Hearn,[20] M. A. Barucci,[21] J. L. Bertaux,[22] I. Bertini,[10] G. Cremonese,[5] V. Da Deppo,[4] S. Debei,[23] M. De Cecco,[24] J. Deller,[12] C. Feller,[21] S. Fornasier,[21] E. Frattin,[5,10] M. Fulle,[25] O. Groussin,[8] P. J. Gutierrez,[26] C. Güttler,[12] M. Hofmann,[12] S. F. Hviid,[7] W. H. Ip,[27,28] J. Knollenberg,[7] J. R. Kramm,[12] E. Kührt,[7] M. Küppers,[29] F. La Forgia,[10] L. M. Lara,[26] M. Lazzarin,[10] J.-C. Lee,[27] J. J. Lopez Moreno,[26] N. Oklay,[7] X. Shi,[12] N. Thomas,[30] C. Tubiana[12] and J. B. Vincent[7]

Affiliations are listed at the end of the paper

Accepted 2017 October 29. Received 2017 October 27; in original form 2017 March 30

ABSTRACT

We provide a three-dimensional model of the inner layered structure of comet 67P based on the hypothesis of an extended layering independently wrapping each lobe. A large set of terrace orientations was collected on the latest shape model and then used as a proxy for the local orientation of the surfaces of discontinuity which defines the layers. We modelled the terraces as a family of concentric ellipsoidal shells with fixed axis ratios, producing a model that is completely defined by just eight free parameters. Each lobe of 67P has been modelled independently, and the two sets of parameters have been estimated by means of non-linear optimization of the measured terrace orientations. The proposed model is able to predict the orientation of terraces, the elongation of cliffs, the linear traces observed in the Wosret and Hathor regions and the peculiar alignment of boulder-like features which has been observed in the Hapi region, which appears to be related to the inner layering of the big lobe. Our analysis allowed us to identify a plane of junction between the two lobes, further confirming the independent nature of the lobes. Our layering models differ from the best-fitting topographic ellipsoids of the surface, demonstrating that the terraces are aligned to an internal structure of discontinuities, which is unevenly exposed on the surface, suggesting a complex history of localized material removal from the nucleus.

Key words: methods: data analysis – comets: general – comets: individual: 67P/Churyumov–Gerasimenko.

1 INTRODUCTION

ESA's *Rosetta* spacecraft provided the unique opportunity to perform a detailed analysis of the nucleus of comet 67P/Churyumov–Gerasimenko (67P) thanks to the wide number of frames acquired during the 2-yr mission. The onboard camera system OSIRIS (Optical, Spectroscopic, and Infrared Remote Imaging System), which comprises a Narrow Angle Camera (NAC) for investigation of nucleus surface and a Wide Angle Camera (WAC) for gas and dust studies (Keller et al. 2007), allowed the identification of an unexpectedly complex surface morphology (Thomas et al. 2015), dominated by circular pits generated by endogenic activity (Vincent et al. 2015), fractures at all scales (El-Maarry et al. 2015a; Groussin et al. 2015; Auger et al. 2015), scattered boulders (Pajola et al. 2015, 2016a), gravitational deposits produced by the collapse

⋆ E-mail: luca.penasa@gmail.com (LP); matteo.massironi@unipd.it (MM)

of cliffs (Pajola et al. 2017) and ordered sets of terraces and mesas (Massironi et al. 2015; Thomas et al. 2015; Pajola et al. 2016b). Such geological complexity is also reflected by the large number of regions (26) in which a relatively small body as the comet 67P has been subdivided (El-Maarry et al. 2016, 2017).

Comet 67P is characterized by a peculiar bilobate shape: the larger lobe, hereafter the big lobe (BL), has a size of $4.1 \times 3.3 \times 1.8$ km, while the small lobe (SL) is approximately $2.6 \times 2.3 \times 1.8$ km wide (Jorda et al. 2016). The BL and the SL are connected by a bridge of material ∼2.2 km long and ∼0.8 km wide which is known as the *neck*. The shape of the comet nucleus, its activity, and the surface morphology, as observed by OSIRIS cameras during the *Rosetta* mission, are described by Sierks et al. (2015) and Thomas et al. (2015). The two lobes are thought to be the result of a non-destructive impact which joined two independent objects (Massironi et al. 2015; Jutzi & Benz 2017).

One of the major discoveries about 67P is the presence of morphological features that can be related to layered material, constituted by ordered set of terraces and mesas. Using these morphologies as a proxy for the local orientation of the inner structure, Massironi et al. (2015) produced geological cross-sections of the Northern hemisphere of the cometary body, providing pieces of evidence for a large-scale layering of the nucleus, independently wrapping each lobe. This finding suggested a separated evolution of two bodies that joined together in a non-destructive collision. In that work the terraces were interpreted as the surfaces of discontinuity which separate the layers. Other observations by Rickman et al. (2015) and Marchi et al. (2015) reinforced a view of a globally layered body, where the layers are not local and shallow-surface features but are instead expression of an extended inner structure.

The existence of potentially layered materials is also documented for other Jupiter-family comets (Bruck Syal et al. 2013; Cheng, Lisse & A'Hearn 2013), although the possible process leading to layers formation remains unclear. Observations made on Tempel-1 led to the idea that layers might be the results of the accretion process itself (Belton et al. 2007).

Davidsson et al. (2016) suggests that denser external layers might be the results of an increase in collision velocities during the cometesimal formation: denser layers would thus wrap an inner porous core. Jutzi & Benz (2017) proposed that the layers might be the direct result of the lobe-forming impact: after the initial disruption, subsequent re-accumulation might have led to the formation of a layered sequence.

Geomorphological maps of 67P show that the presence of layering-related morphological features is common in the Northern hemisphere (Giacomini et al. 2016) as well as in the Southern one (Lee et al. 2017). These analyses supported the idea of a globally layered structure although did not allow the three-dimensionality of the layering to be clearly constrained.

In this paper we describe the work done so far to investigate the morphology of 67P and its potential connection with the geometry of an inner layered structure of global extension.

By measuring the orientations of the observed flat terraces and mesas on the latest comet nucleus shape model, we have generated a simplified 3D model of closed surfaces containing the flats themselves. This model is able to consistently predict the orientations of terraces and mesas and to trace the predicted intersection of the discontinuities on the surface, enabling the identification of the morphologies which might be related to the layered structure.

We proceed by showing some of the morphologies which have been linked to the layering with the aid of the three-dimensional shape model, with special attention to the terraces. In the methodological section, the procedures used to quantify and to model the orientations of terraces are then presented. Results of the modelling, their connection with the observed morphologies and their implications in terms of the nucleus internal structure are then discussed in the concluding sections.

2 LAYERING-RELATED MORPHOLOGIES

For our analysis we used two different shape models of 67P. The first is computed by means of photoclinometry technique (SPC) by Jorda et al. (2016) and the second was produced through stereophotogrammetic methods (SPG, Preusker et al. 2015; Preusker et al. 2017) from images collected by OSIRIS cameras (Keller et al. 2007). The computations were made on the SPG full-resolution global triangular mesh provided by Preusker et al. (2017), the cg-dlr_spg-shap7-v1.0 shape model, composed of more than 40 million facets with a typical point spacing of 1–2 m. For all snaphots in this manuscript we used a reduced version of this model.

To better understand the observed features within their gravitational context, we computed the gravitational slopes as the angle between the local surface normal and the opposite vector of the estimated acceleration field. We employed the Werner's method (Werner 1994) to compute the local gravity vector, considering the body made of homogeneous material with a density of 532 kg m^{-3} (Jorda et al. 2016). Gravity was computed using a reduced version of the shape model, composed of 500 000 facets. The contribution of centrifugal forces due to the body's rotation, considering a rotation period of 12.4043 h (Sierks et al. 2015), was then added obtaining an estimate of the total acceleration field on the surface.

The high-slope regions are aligned in laterally persistent cliffs (see Fig. 1 a and Section 3 of the supplementary material) which are stacked on top of each other, forming series of planar terraces separated by almost-vertical cliffs. Terraced terrains, which are present both in the Northern and in the Southern hemisphere at a variety of scales, clearly represent a morphological oddity for their consistent coupling with elongated high-slope regions (cliffs), their ordered and repetitive stair-case pattern and their parallelism with linear traces that can be observed on the cliffs and inside pits (see also Massironi et al. 2015; Thomas et al. 2015; Vincent et al. 2015).

Fig. 1(b) shows a topographic profile of 67P, obtained by cutting the three-dimensional shape model across y–w in Fig. 1(a), thus the resulting cross-section spans from Anhur to the Imhotep flat, passing through the Bes top, which constitutes a mesa. The clear alternation between flats and cliffs is further highlighted in Fig. 1(c) where their average orientations have been traced with segments of different colours (blue for the terraces and red for the cliffs).

The flat segments can be extended inside the nucleus, as shown in Fig. 1(c), allowing to correlate terraces at the opposite sides of the elevated Bes area. This suggests that the surfaces corresponding to the terraces must indeed continue inside the nucleus, in the form of three-dimensional curved surfaces.

Under this view two consecutive terraces define a tabular element, or *layer*, which is curved and bounded by two discontinuities, which are materialized on the surface by the terraces themselves. Stacks of layers appear to be repetitive and ordered. In some cases the layer-defining discontinuities can be directly observed on cliffs as linear traces, consistently aligned with the nearby terraces (Thomas et al. 2015).

A similar explanation was also provided by Rickman et al. (2015) and Marchi et al. (2015), who observed the coincidence of planar features at the opposite sides of elevated terrains, although they simplified their geometry as planes. Massironi et al. (2015) and Lee

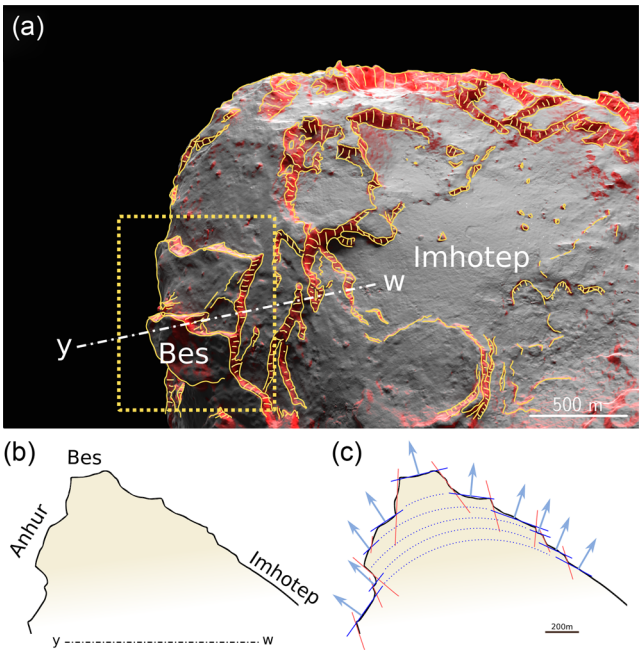

Figure 1. (a) A render of the three-dimensional shape model by Preusker et al. (2017), centred on the Imhotep region on the BL. High-slope regions (>35°) have been shaded in red and highlighted in yellow to demonstrate their elongated and laterally persistent geometry. It is evident that cliffs and terraces create a staircase pattern. (b) Topographic profile obtained cutting the model along the y–w direction from Bes towards Imhotep region further illustrates the alternation of flats and cliffs. In cross-section (c) cliffs and terraces are highlighted by red and blue lines, respectively. Arrows illustrate how the terraces change orientation along the topographic profile. To maintain coherent these orientations the surfaces forming the terraces must indeed be curved within the nucleus interior. ImageID reference: `WAC_2016-07-02T10.41.45.806`.

et al. (2017) drew possible geological sections of the internal layered geometry of 67P by interpreting the terraces as the morphological expression of bedding planes organized in independent onion-like structures for the two lobes.

3 METHODS

3.1 Terraces mapping

Terraces appear to be the most evident feature suggesting an inner layering: they are widespread all over the comet surface and they present a variable areal extension, depending on the scale of observation.

We identified as many terraces as possible on both the lobes by tracing their boundaries on the nucleus shape model.

We followed the subsequent criteria to identify a valid terrace:

(i) it must appear planar;
(ii) it must exhibit a typical geometry, bounded by cliffs or steep slopes and being part of a set of terraces.

Following these criteria a *mesa* is considered a special case of a terrace, bounded on all sides by cliffs. We underline that terraces are not necessarily gravitationally flat, although this is a common feature (see also Massironi et al. 2015). We detected 250 and 233 terraces on the BL and on the SL, respectively (Fig. 2).

For each identified terrace or mesa we computed a reference orientation, by extracting the vertices of the shape model within the mapped boundary and computing the best-fitting plane, using the same methods used by Massironi et al. (2015). The best-fitting plane provides a unit normal $\hat{\boldsymbol{n}}_{\rm terr}$, while the centroid of the fitted vertices provides a reference point $\boldsymbol{p}$ for localizing the observation.

In addition to the measurement errors, the estimated orientation of a terrace is also affected by additional errors that must be considered: for example, the best-fitting normal is only an approximation of the original orientation of the discontinuity surface, because of possible erosive and depositional phenomena that might have modified its geometry (Fig. 3).

3.2 Modelling the terrace orientations

By following the work by Massironi et al. (2015), we decided to verify the possibility that these terraces represented the exposed discontinuity surfaces of a pervasive structure characterizing the two lobes of 67P. To reach this goal we modelled each flat terrace as an ellipsoidal surface, belonging to a family of concentric ellipsoids, with constant axis ratios. Each lobe is independently modelled by a different family of ellipsoidal shells.

We based our choice on the idea that the layers form shells wrapping the nucleus, one on top of each other, defining *onion-like* curved envelopes that can be approximated by triaxial ellipsoids.

To derive an analytical expression for the model, we first considered the generic ellipsoid centred in the origin and with unitary a-axis length:

$$\frac{x^2}{a^2}+\frac{y^2}{b^2}+\frac{z^2}{c^2}=1, \quad \text{with} \quad a>b>c \quad \text{and} \quad a=1, \tag{1}$$

where x, y, z are the coordinates of a generic point $\boldsymbol{p}$ on the ellipsoid surface. We then considered the family of ellipsoids concentric to this one, whose axes are all proportional to the same scaling factor λ:

$$\frac{x^2}{\lambda^2}+\frac{y^2}{(\lambda b)^2}+\frac{z^2}{(\lambda c)^2}=1. \tag{2}$$

This equation defines an infinite number of ellipsoidal shells, one for each $\lambda > 0$, all of them sharing the same axial ratios, which correspond to the b and c parameters. Solving for λ, we obtain

$$\lambda=\frac{1}{bc}t=f(\boldsymbol{p}), \quad \text{where} \quad t=\sqrt{b^2c^2x^2+b^2z^2+c^2y^2}. \tag{3}$$

This function thus associates a specific scalar value λ to the point $\boldsymbol{p}$, which is then used in equation (2) to explicitly obtain the equation of the ellipsoidal shell passing for that point. The normal of the shell passing for $\boldsymbol{p}$ corresponds to the gradient of $f(\boldsymbol{p})$:

$$\boldsymbol{n}_{\rm ell}=\left[\frac{bcx}{t},\frac{cy}{bt},\frac{bz}{ct}\right]^{\rm T}=\nabla f(\boldsymbol{p}) \tag{4}$$

This formulation for a family of ellipsoidal shells has the advantage, over other possible choices, to have a simple analytical solution.

In the more general case, the family of ellipsoids is not centred in the origin and can be arbitrarily oriented in space. We can thus generalize the modelling equations (2) and (4) to account for a centre $\boldsymbol{c}=[c_x, c_y, c_z]^{\rm T}$ of the ellipsoid other than the origin, and an arbitrary orientation provided by the rotation matrix $\mathbf{R}$, so that λ becomes

$$\lambda=f(\mathbf{R}^{\rm T}\cdot(\boldsymbol{p}-\boldsymbol{c})) \tag{5}$$

and the gradient

$$\boldsymbol{n}_{ell}=\mathbf{R}\cdot\nabla f(\mathbf{R}^{\rm T}\cdot(\boldsymbol{p}-\boldsymbol{c})). \tag{6}$$

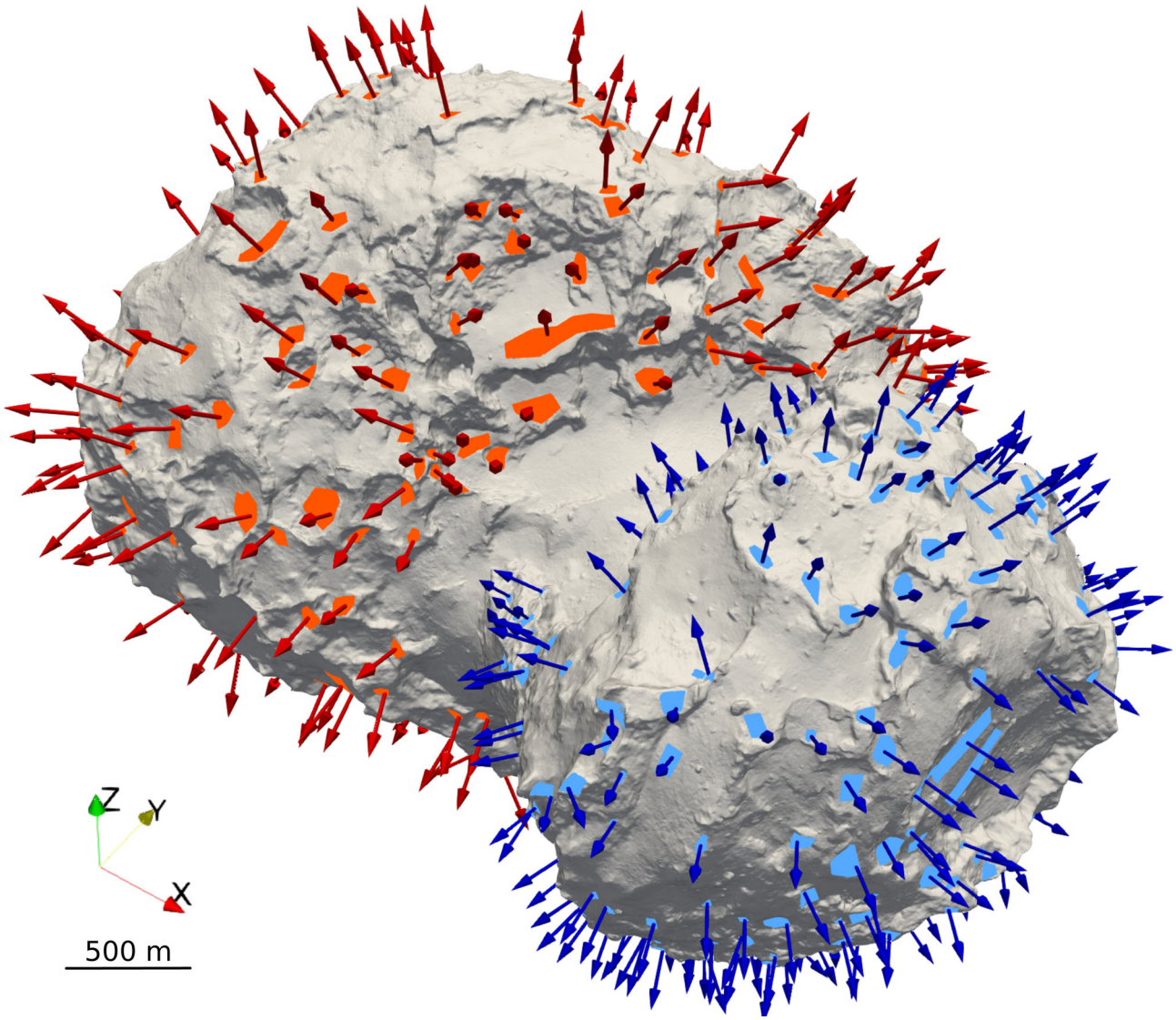

Figure 2. Visualization of the terraces identified on the BL (255) and the SL (239). For each terrace a point in space and the correspondent best-fitting plane normal were estimated. In blue the observations on the SL and in red the ones on the BL. For interpretation of the colours in this figure, the reader is referred to the web version of this article.

The rotation **R** can also be parametrized as a triplet of angles α, β, γ (see e.g. Diebel 2006), describing the orientation in terms of subsequent rotations around the ellipsoid's axis (i.e. Yaw, Pitch and Roll). Construction of the matrix **R** from the three angles, together with PYTHON code for model evaluation, is reported in Section 1 of the supplementary material.

In the following, we will refer to the model defined by equations (5) and (6) as the ellipsoidal model (EM), and to the scalar value λ obtained from equation (5), as the reference-ellipsoid semimajor axis (RES).

The proposed model allows to use the RES value as a metric of *distance* from the centre of the ellipsoidal shells. For example, the difference $\lambda_2 - \lambda_1 = f(\boldsymbol{p}_2) - f(\boldsymbol{p}_1)$, for two points $\boldsymbol{p}_1$ and $\boldsymbol{p}_2$, on two different terraces, returns the separation calculated along the a-axis of the two corresponding shells.

The complete ellipsoid-based model is thus defined by a parameter vector of eight values:

$$\boldsymbol{x} = [c_x, c_y, c_z, a, b, \alpha, \beta, \gamma]^{\mathrm{T}}, \tag{7}$$

three parameters for the coordinates of the centre, two for the axial ratios, and three for the orientation.

For each mapped terrace we can define an angular value θ, corresponding to the misalignment of the terrace from the model's prediction:

$$\theta = \arccos\left(\frac{\boldsymbol{n}_{\mathrm{ell}}}{|\boldsymbol{n}_{\mathrm{ell}}|} \cdot \hat{\boldsymbol{n}}_{\mathrm{terr}}\right), \tag{8}$$

where $\boldsymbol{n}_{\mathrm{ell}}$ is the vector representing the modelled orientation provided by equation (6) and $\hat{\boldsymbol{n}}_{\mathrm{terr}}$ is the actual orientation of the terrace, as estimated on the shape model.

To estimate the parameters, their standard errors and to test the uniqueness of the solution, we adopted a bootstrap approach (Efron 1979; Chernick 2008): the input data set of observations was resampled with replacement 10 000 times, simulating the results that might come from a different observation collection campaign.

By means of a non-linear optimization performed using the *Ceres* solver (Agarwal et al. 2016), we computed the parameters for the best-fitting EMs at each iteration by minimizing the sum of the θ^2

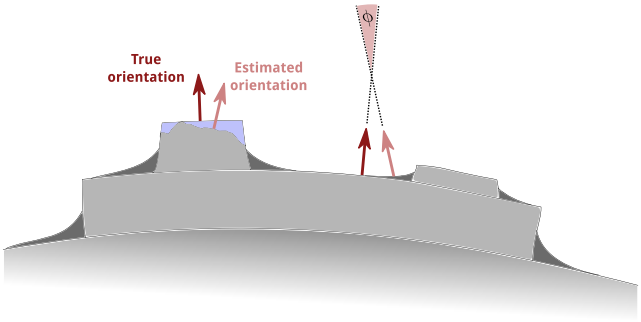

Figure 3. Talus and eroded surfaces introduce uncertainties into the estimated attitudes, here represented by the ϕ angle. Notice that these errors are likely to be larger than the numerical error introduced by the vertex-fitting procedure, which is estimated to be lower than 5° (Massironi et al. 2015).

angles:

$$\min_{\mathbf{x}} \quad \sum_{i=0}^{k} \theta_i^2, \tag{9}$$

where k is the total number of observations to be fitted. This procedure provided 10 000 different possible parameters vectors for each lobe, whose distributions are shown in Fig. 4. From these distributions, we computed the parameters maximum likelihood estimates (MLEs) and the respective standard errors, which provided the *reference solutions* reported in Table 1. These parameters fully define two EMs in the *Cheops* reference frame (Preusker et al. 2015) which are used to describe the layered structure of the two lobes.

4 RESULTS

Table 1 summarizes the reference solutions of the parameters for the two EMs. Each model defines a family of ellipsoids with fixed b/a and c/a ratios, which correspond to the b and c parameters reported in Table 1. The parameters c_x, c_y, and c_z are the centres of the ellipsoids and α, β, and γ are Yaw, Pitch, and Roll angles, describing their orientation in space.

Angular residuals for the reference solutions show that the EMs explain the observations with a misalignment which is lower than 18° for most of the terraces. Full histograms of the residuals are reported in Fig. 1 of the supplementary material.

Notice the large values for the estimated 2σ error for the γ angle for the SL: this is due to the fact that the resulting ellipsoid is substantially a rotational ellipsoid (b and c are equal considering the 2σ confidence intervals), thus allowing for a broader range of solutions in terms of γ angle. On the contrary, the EM of the BL shows an evident triaxiality and consequently the 2σ value for the γ angle is lower.

A comparison between the centres of the best-fitting topographic ellipsoids (white arrows in Fig. 4), obtained from the SPC shape model by Jorda et al. (2016) and our EMs, shows a significant shift of 284 and 508 m, respectively, for the BL and the SL centres (see also the values reported in Section 2 of the supplementary material).

Parameters of Table 1, coupled with equation (5) and some additional calculations can be used to estimate the values of RES for each of the vertices of the 3D shape model. This must be done separately for the two lobes. Fig. 5 provides a visual representation of the three-dimensional EMs and their intersection with the nucleus surface. Vertices of the shape model laying at the same RES are predicted to be part of the same layer. Contour lines thus correspond to the intersection of the ellipsoidal shells with the nucleus surface, providing a visual clue of the local orientation of the layering and a possible global correlation of distant terrains. When contour lines are closely spaced, the layers are predicted to emerge from the nucleus at a high angle with the local topography. On the contrary, lines that are spaced far apart represent layers that are either emerging at a low angle or exposing the layer-forming discontinuity itself.

RES values computed for the nucleus interior allow cross-sections to be produced as shown in Fig. 6. Notice that the intersections of ellipsoidal shells with the section plane shown in the figure (dashed lines), as well as the contour lines of Fig. 5, do not represent any specific discontinuity recognized on the nucleus, but must be regarded as a simplified representation of the local orientation of the layering, as predicted by our model. The global continuity of these surfaces, their relation with our model, and some possible geometrical arrangements of layers will be discussed in detail in Section 6.

The range of RES values on the BL goes from 1.4 to 2.6 km and from 0.72 to 2.1 km on the SL. The deep interior of the comet (corresponding to depths lower than 1.4 for the BL and 0.72 km for the SL) is not exposed anywhere on the surface. The total thickness of the visible layered sequences is thus of about 1.2 and 1.38 km for the BL and the SL, respectively.

5 COMPARISON WITH OBSERVED MORPHOLOGIES

The EM can be used to predict the local orientation of layering and the general aspect we can expect to observe on the surface, depending on the angles at which the layering encounters the topographic surface.

Surface pieces of evidence of the inner layering are constituted by both linear traces, which might be visible wherever the topography is cutting the layers at a high angle, and locally *flat* terrains, in the form of *mesas* or *terraces*, which are expected to be parallel to the local layer orientation predicted by our model.

We thus used selected OSIRIS images for validating our modelling results. For each selected OSIRIS image, we rendered a synthetic picture of the nucleus from the same point of view of the camera and with the sun lighting the shape model at the same orientation as it was at the time of image acquisition. We used the computed gravitational slopes to artificially colour the major cliffs on the comet. To better represent the model predictions and to produce uncluttered figures, we traced on the shape model the predicted layer intersection with the nucleus surface (in the form of RES contour lines) wherever the two following conditions are simultaneously satisfied:

(i) the layer is predicted to encounter the surface at an angle greater than 25°, to exclude regions where the layering is not expected to be well exposed in the form of linear traces;
(ii) the gravitational slopes are greater than 35°, to exclude those regions that are likely covered by dust and would not allow the underlying layering to be observed.

Some of the images used have been previously discussed in literature (see Massironi et al. 2015; Rickman et al. 2015; El-Maarry et al. 2016; Giacomini et al. 2016; Lee et al. 2017); thus additional details about the general context and the previous interpretations can be found in the related references.

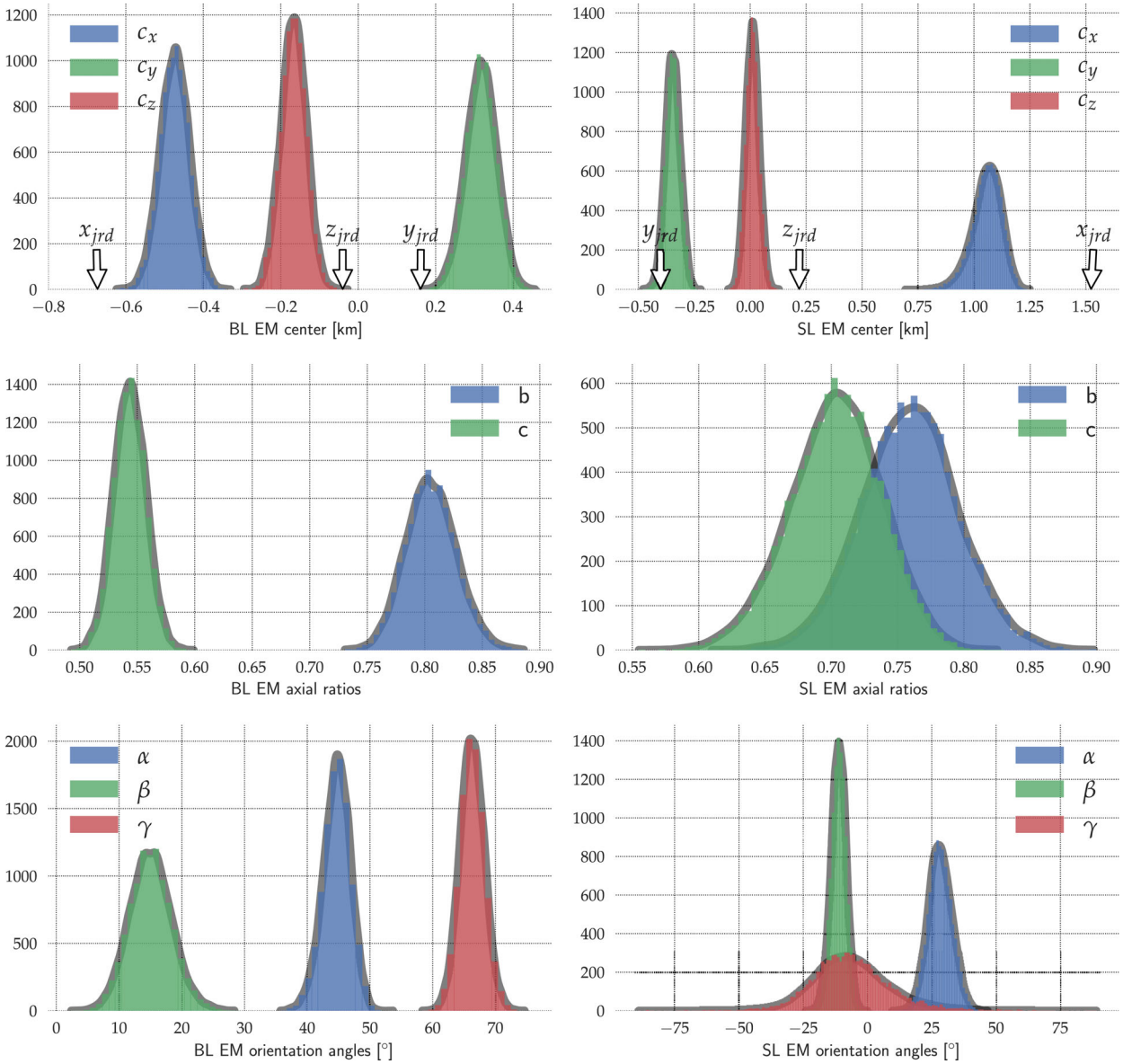

Figure 4. Histograms of the parameters obtained by the bootstrap iterations for the BL (left column) and for the SL (right column) from which the reference solutions of Table 1 were obtained as the median values. The parameters c_x, c_y, and c_z are the coordinates of the centre of the EM, b, and c their axial ratios, while α, β, and γ are the Yaw, Pitch, and Roll angles. Coordinates of the centre of the best-fitting topographic ellipsoid, as resolved by Jorda et al. (2016), are plotted as white arrows. For interpretation of the colours in this figure, the reader is referred to the web version of this article.

An additional set of 12 OSIRIS images that can be used to compare the model's prediction with the observed morphologies can be found in Section 4 of the supplementary material.

5.1 Small lobe

The section in Fig. 6(a) illustrates the peculiarity of the *Hathor* region. The Hathor cliff morphology has been previously discussed by Thomas et al. (2015), Rickman et al. (2015), Groussin et al. (2015) and El-Maarry et al. (2015a) for the singular lineations that can be observed, which have been previously interpreted as a set of vertical fractures perpendicular to the traces produced by an inner layering.

Actually, the cliff cuts the SL EM at a rather high angle with respect to local ellipsoidal surfaces, exposing the layers along their

Table 1. MLEs of the EM parameters and relative 2σ errors, for both the BL and the SL.

Parameter[a]	BL	2σ	SL	2σ
c_x	−0.473	0.076	1.06	0.13
c_y	0.32	0.08	−0.346	0.066
c_z	−0.167	0.066	0.01	0.059
b	0.805	0.044	0.76	0.073
c	0.544	0.028	0.704	0.069
α	44.8	4.3	28.1	9.3
β	15	6.7	−11.2	5.7
γ	66.3	3.9	−7.3	34.4

[a] Distances in km and Tait–Bryan angles in degrees, following the *intrinsic z–y'–x"* convention. Everything in the *Cheops* reference frame (Preusker et al. 2015). b and c are the axial ratios with respect to the a-axis.

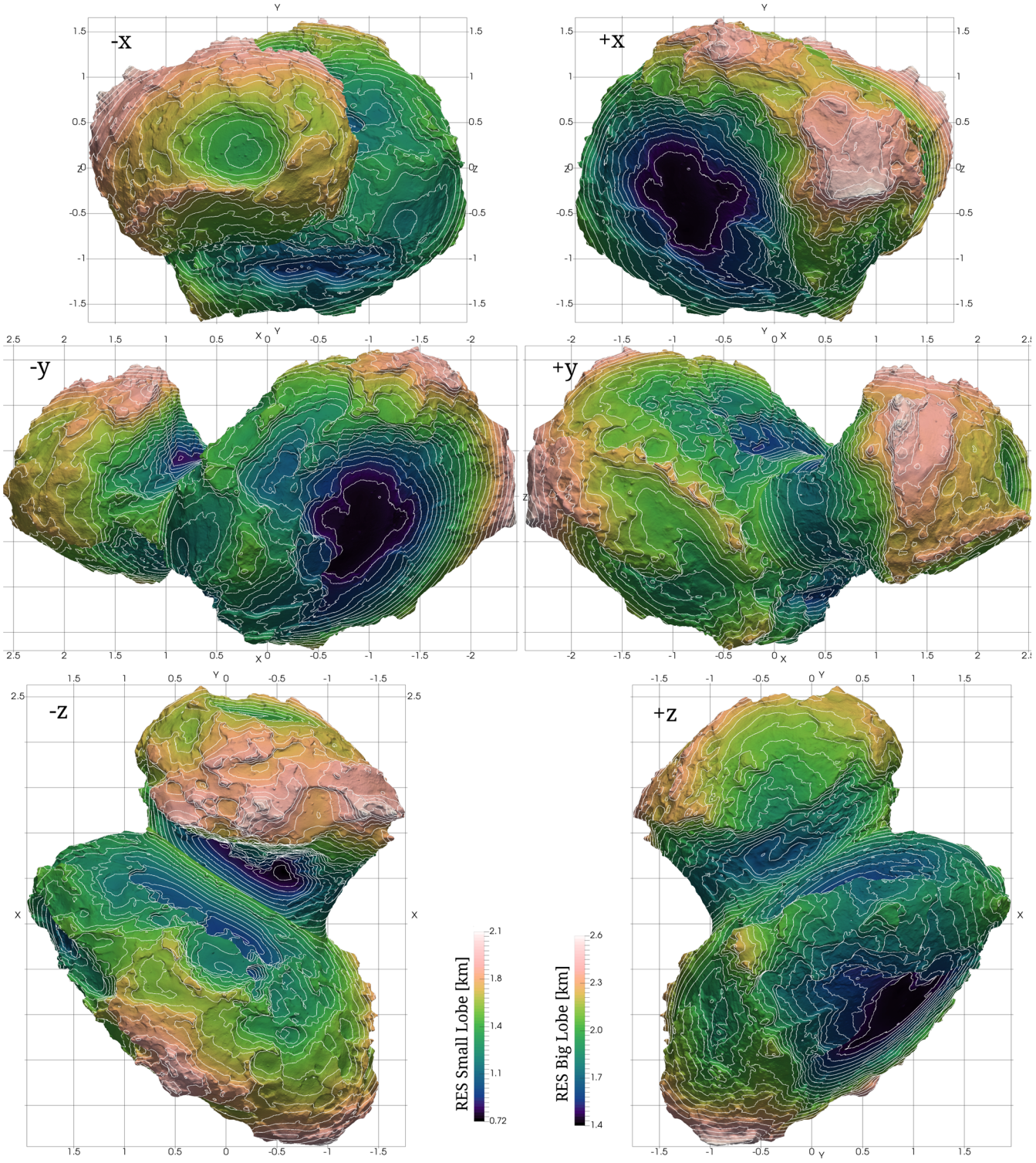

Figure 5. The RES predicted by the models can be used as metric for evaluating the relative position of any point on the surface, in terms of layer superposition. Vertices located at the same structural level have the same colour. Considering the onion-like conceptual model by Massironi et al. (2015), each contour line (in white), corresponds to a specific shell. Contour lines are traced every 50 m of RES, letters correspond to the viewing direction in the Cheops reference frame. For interpretation of the colours in this figure, the reader is referred to the web version of this article.

shortest dimension, thereby showing the layers thickness. This result is confirmed by Fig. 7 which shows both the linear features traced by Thomas et al. (2015) and the geometry of the modelled ellipsoidal shells at the surface.

A very good correlation is evident between the observed features at the Hathor surface and the contour lines of the layers at the surface. Our model shows that Hathor is the region with the best and larger exposure of layers on the whole cometary body.

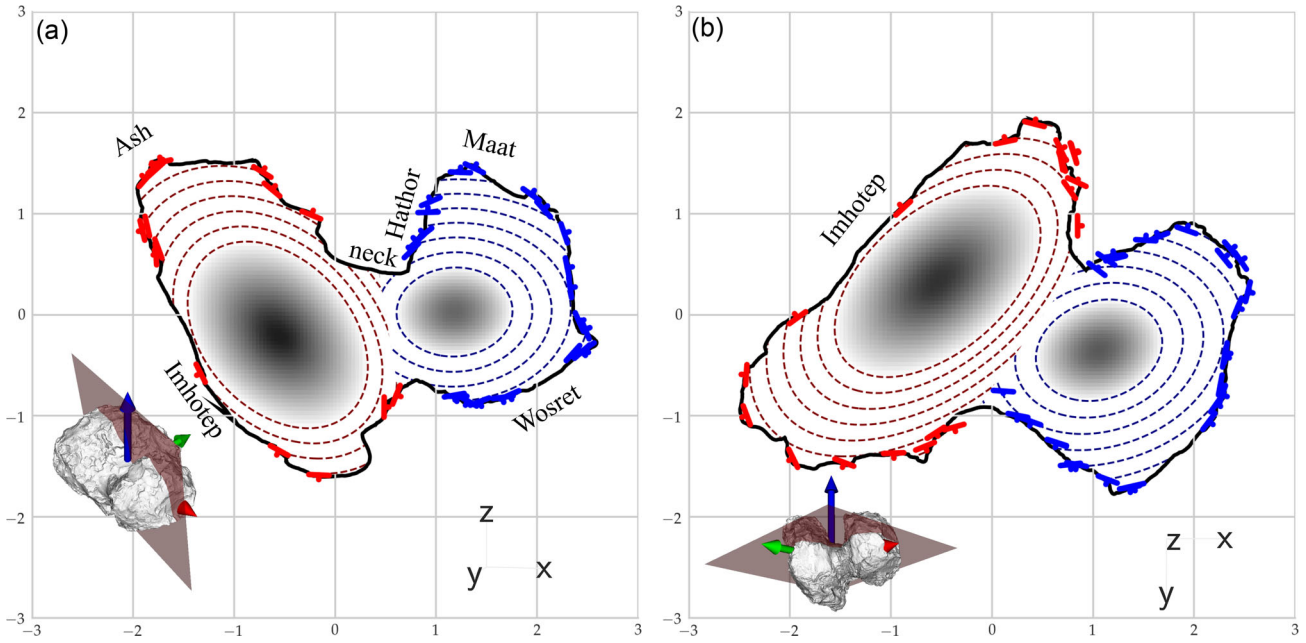

Figure 6. Cross-sections cutting through the nucleus. The black line represents the shape model at the section plane. A small number of observations near the section plane have been plotted with a red mark for the BL and a blue one for the SL. In grey the interior part that has no surface expression (not outcropping). Dashed lines represent the shells derived from the EM, with a relative spacing of 200 m. Distances are in km on the section plane. The insets show the position of the section plane on the SPC model. For interpretation of the colours in this figure, the reader is referred to the web version of this article.

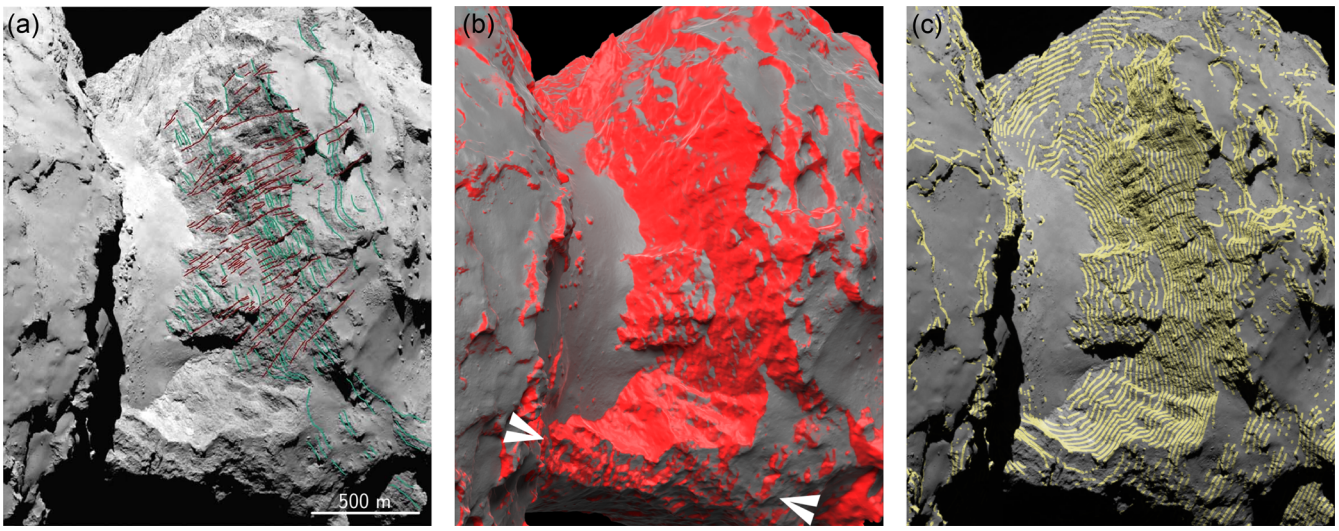

Figure 7. The Hathor cliff. In (a) the original figure of Thomas et al. (2015) (see also Rickman et al. 2015) with highlighted in green and brown two sets of perpendicular linear features. Brown lines run *'upwards for much of the height of the cliff'*, while green lines are described as *'linear features aligned with small terraces, which might suggest inner layering'*. The presence of terraces and of corresponding high slopes is evident in (b) where slopes $>35^\circ$ have been coloured in red. In (c) the modelled orientation of the layer traces on the cliff, as computed using the EM for the SL. The two arrows in the centre image show a continuous terrain composed of superimposed terraces, that appear to be in continuity with the structure of the SL. ImageID reference: `NAC_2014-08-07T20.37.34.564`. For interpretation of the colours in this figure, the reader is referred to the web version of this article.

Hathor faces the nucleus neck region, which is probably the most complex layered structure to interpret, since the SL and the BL join, and the layers intersect each other. In this region the terraces appear to maintain the original information about the layered structure of two independent lobes, although a large portion of the SL has been lost.

Fig. 8(a) shows the Southern hemisphere (Wosret region) of the SL as captured by the NAC camera. Several parallel linear features were identified by Lee et al. (2017) and interpreted as the possible expression of the inner layering.

When compared with the corresponding EM for the SL (Fig. 8b), these linear traces are in good agreement with the overall layer orientation predicted by the model. Notice that the EM have been fitted by using terrace orientations only, and no linear features were used for determining the models.

5.2 Big lobe

As described in Section 4 the EM for the BL is significantly shifted with respect to the corresponding best-fitting topographic ellipsoid.

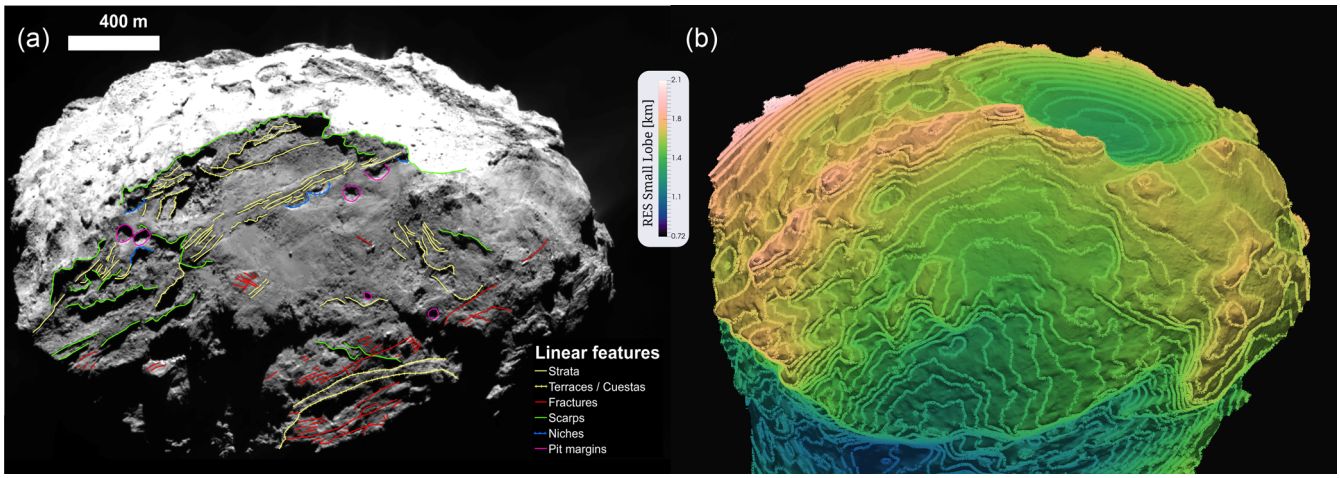

Figure 8. In (a) NAC image showing the map of linear features identified by Lee et al. (2017) in the Wosret region (Southern hemisphere of the SL). In (b) the corresponding shape model coloured by the RES scalar field computed from the EM of the SL. Contour lines represent the traces produced by the intersection of a set of evenly spaced ellipsoidal shells defined by our model. ImageID reference: `NAC_2015-05-02T10.42.52.535`. For interpretation of the colours in this figure, the reader is referred to the web version of this article.

This is due to the fact that the layers on the BL have been subject to a non-uniform removal process which left exposed both *shallow* and *deep* layers. This structure can be appreciated in Fig. 9. The colours are here used to represent the modelled RES for each pixel of the OSIRIS image.

It can be seen in this figure that the most external layers have been preserved only in small portions of the comet: they are circled in Fig. 9(a) and are coloured in pink to white (and highlighted by an arrow) in Fig. 9(b). These areas represent the latest remnants of the most external layers which have now been almost completely lost. They remain in the form of *mesas* and are unequivocally related to layered terrains. At the same time also much deeper layers are exposed on the BL: they are depicted in bluish colour in Fig. 9(b), and essentially correspond to the Imhotep region, where a single specific layer seems to be present at its basis.

The Imhotep region has been described as an extremely smooth surface which is enclosed on its boundaries by elevated rims made of consolidated materials shows evidences of terracing (El-Maarry et al. 2015b). Our model well explains this structure: the central part of the Imhotep region constitutes one of the deepest exposures of an inner shell of the *onion-like* layering of the 67P nucleus. On the boundaries of this surface the material is layered, creating structures whose elevated tops are reached through a series of staircase terraces, demonstrating the layered nature of the terrains. In practice, from a structural point of view, the Imhotep region can be considered as a valley, exposing deep layers, surrounded by *mountains* whose shallower tops can be up to 1.2 km higher and are constituted by the Ash and Apis regions (Fig. 9a).

Mesas and *terraces* are common on the BL at a variety of RESs, although in the Southern hemisphere only terrains at a deeper level are preserved, with respect to the highest mesas in the Northern hemisphere (see e.g. Fig. 5).

Finally, the BL, in contrast with what is observed in the Hathor region of the SL, does not present any extended surface cutting at high angle the internal layering: thus it exhibits the inner layering mostly as staircase patterns of terraces. However, linear traces connected with the layering can also be found here at a small scale, on cliffs and on pits walls, as can be seen for example in Fig. 10.

5.3 Neck region

The *neck* region, which is a highly depressed terrain determining the overall bilobate shape of 67P, has been previously described as the junction between two independent cometesimal which joined together after a non-destructive collision (Massironi et al. 2015; Jutzi et al. 2017). Since our model has been developed under this specific assumption, we want to verify the possible agreement between the modelled layered structure and the corresponding observed morphological features, found in both OSIRIS images and in the 3D shape model.

Fig. 11 illustrates a peculiar alignment of blocks-like features in the neck region (in the Northern hemisphere, the *Hapi* region), that was previously described by Pajola et al. (2015). Fig. 11(a) shows the geopotential (total potential energy, obtained by considering the contribution of the gravitational and rotational forces), at the centre of Hapi. The contour lines of the potential trace a curved topographic ridge, apparently constituted by aligned boulders.

Figs 11(b) and (c) show that the ridge is in geometric continuity with the set of terraces coloured in blue, while a second set of terraces, located at a deeper structural level can be identified (in yellow in the figure). The white arrows in Fig. 11(b) show two morphological structures that can be interpreted as a small *mesa* (1) and a terrace (2), which is bounded on one side by a small elongated cliff. This structure is likely a partially buried layer of material, emerging from the dust blanket covering Hapi.

This configuration suggests that the peculiar alignment of features that can be observed in the Hapi region is the morphological expression of a buried structure connected with the inner layering of the BL. The geological section in Fig. 6(a) shows that in Hapi the layers encounter the nucleus surface at a high angle, thus exposing the layers as almost vertical elements. Furthermore the concavity of the curved ridge is directed towards the BL, well in agreement with the predicted shape that can be observed in Figs 6(b) and 5. The aligned features can be seen as the remnants of a specific layer of the BL that was emerging in the neck region and has been now completely fragmented in place, into a partially covered ridge, scattered of fragments that might be still physically connected to the underlying structure.

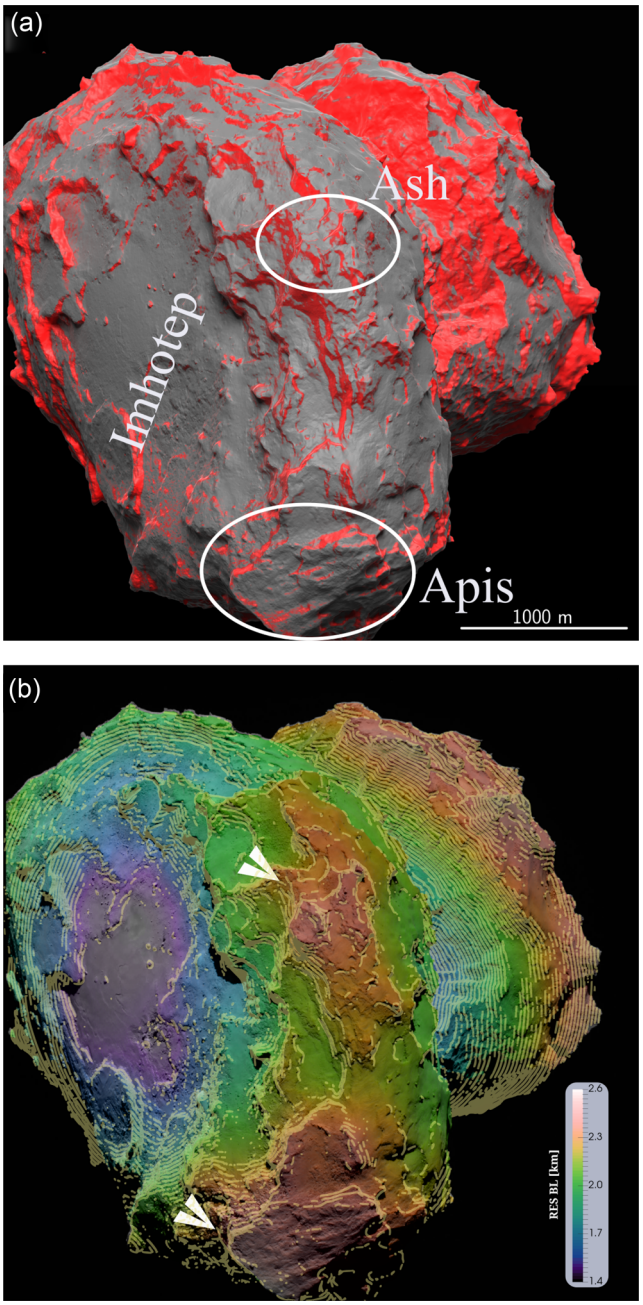

Figure 9. (a) Shape model of the comet nucleus with slopes higher than 35° highlighted in red. Circles show the location on the shape model of the shallower terrains on the BL. (b) Projection of the EM on the same view of the nucleus. The colours are representative of the layer depth in the RES scale, in yellow contour lines of the RES field. Arrows show the same locations circled in (a). ImageID reference: NAC_2014-08-16T14.59.14.556. For interpretation of the colours in this figure, the reader is referred to the web version of this article.

Nucleus cross-sections in Fig. 6 well illustrate the modelled junction geometry for the two lobes which requires that the two layered sequences of the lobes meet each other at varying angles in the majority of the neck region, and are parallel in just a restricted contact area. This geometry can be verified in Fig. 12, which shows an OSIRIS image of the neck (Sobek and Anuket regions) in the Southern hemisphere of 67P, and the respective synthetic image obtained from the shape model, well confirming the model's prediction.

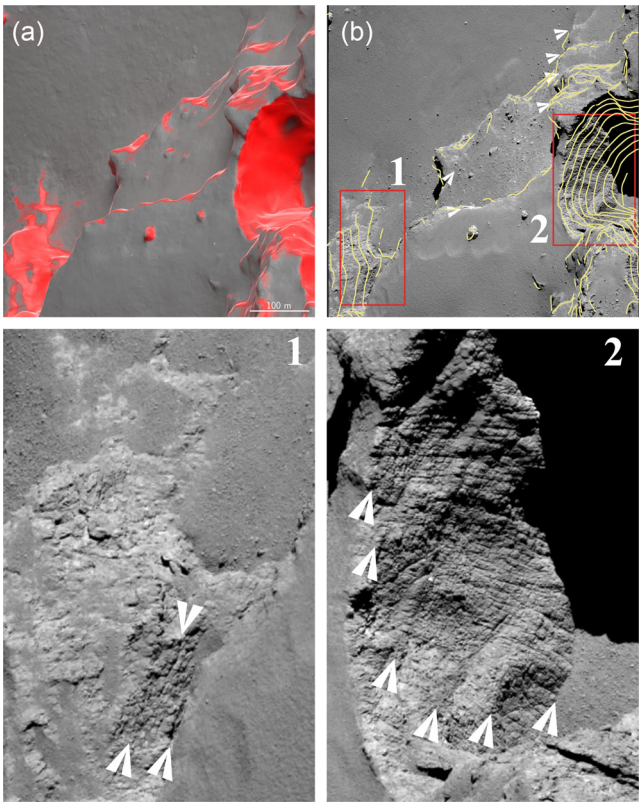

Figure 10. In (a) a synthetic image with cliffs in red and (b) NAC view of the same area on the BL also showing the predicted layers orientations (yellow lines). In the lower panel two close-ups of the NAC picture, showing linear traces on a cliff (1) and inside a pit (2). Outside the pit a set of small terraces (white arrows in b) produce a staircase pattern towards the neck. ImageID reference: NAC_2016-09-30T03.11.30.762. For interpretation of the colours in this figure, the reader is referred to the web version of this article.

Thanks to the opposing structures defined by the layers in Fig. 12 and the observations in the Northern hemisphere of the neck, it is possible to establish pertinence of the neck terrains either to the BL or to the SL. For example, Fig. 7(b) (see white arrows) shows a persistent set of ordered terraces that from the very top of a cliff on the BL extends towards the centre of the neck and stops at the curved ridge in Hapi, suggesting a structural continuity with the BL. We used these pieces of information to obtain a plane of separation between the two lobes, which is used throughout this paper to define the pertinence of the EM (e.g. in Fig. 6).

6 DISCUSSION

Our analysis of the morphological features on the 67P nucleus surface leads us to consider the nucleus, at least until a certain depth, as formed by a series of layers. Each layer is an extended tabular element, which is delimited at the top and at the bottom by two discontinuity surfaces, wrapping the comet interior.

The presence of sets of ordered terraces, which are bounded by elongated cliffs, is one of the main pieces of evidence for the presence of layered material on 67P. These terraces in fact could be interpreted as the result of a morphological process similar to *differential erosion*, acting on the layers themselves. In the specific case, erosion along the vertical direction appears to stop when it encounters the top discontinuity surface of one layer, thus exposing

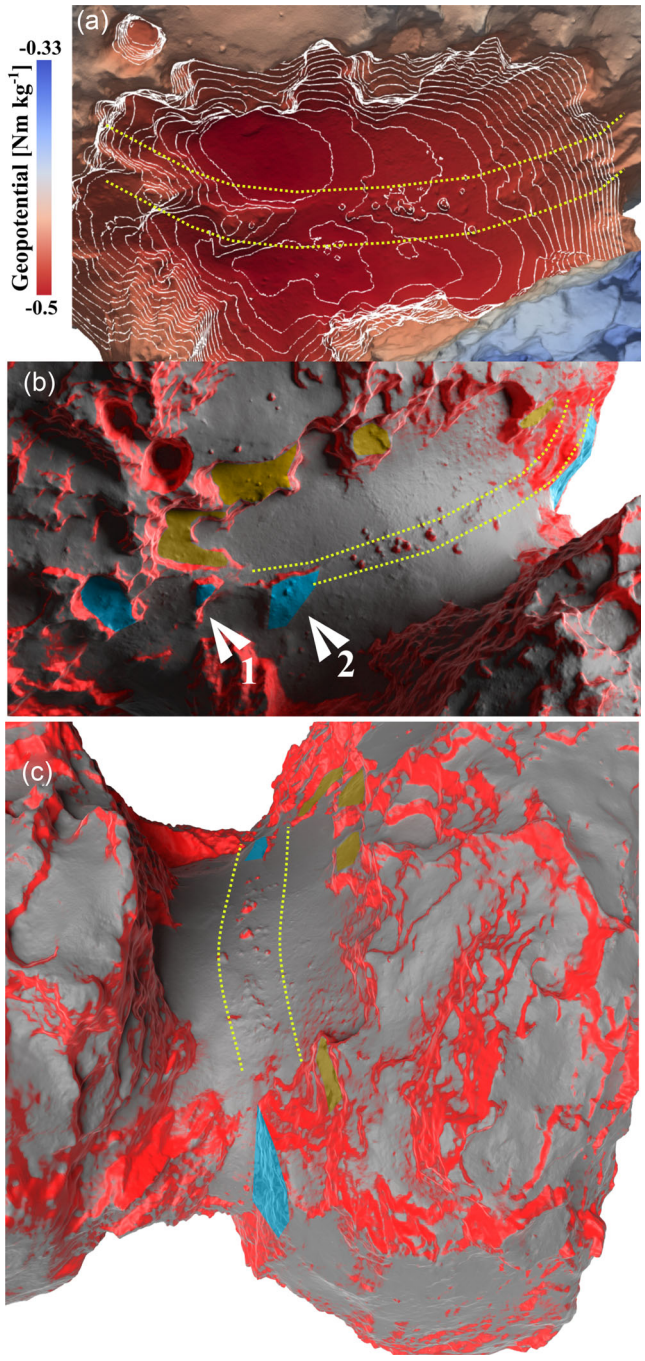

Figure 11. The Hapi region in the neck is characterized by a peculiar alignment of boulder-like features over a ridge. In (a) the geopotential shows that these features are aligned over a morphological ridge, while the potential minima are located at the sides of the ridge (yellow lines). (b) and (c) illustrate the continuity of the ridge with sets of terraces at both ends of the ridge. The concavity of the curved trace described by the outcropping features is directed towards the BL suggesting a structural continuity with the layers of that lobe. For interpretation of the colours in this figure, the reader is referred to the web version of this article.

the flat surface. At the same time, horizontal erosion appears to act much more efficiently on the exposed *head* of the layers, starting a recession process that gradually removes material while still maintaining steep cliffs.

Another evidence of the presence of the layered structure is that whenever the layer discontinuity surface encounters the topographic surface at a high angle, they can be observed as persistent and parallel linear traces, aligned with the terraces.

The evidence for a very large extension of these layers, that encouraged us to model them as wrapping the entire lobes, is demonstrated by the persistence and the continuity of elongated vertical cliffs on the nucleus, as well by the presence of extensive linear features observed in the Hathor cliff. Another good example is the overall geometry of the Imhotep region on the BL that our model predicts to be the largest exposed discontinuity surface of a single layer. It extends for more than 0.8 km^2 (Thomas et al. 2015) and corresponds to the deepest exposed layer of the BL. Throughout the entire cometary nucleus, terraces and linear features consistently follow the prediction of our 3D model, as can be observed for the linear features in Fig. 8. No major inconsistencies between the observed features and the model prediction were found.

An interesting aspect of this analysis is that not only do the obtained EMs for each lobe differ from the respective best-fitting topographic ellipsoids, but also their centres are shifted by few hundred metres with respect to the latter. This finding implies that the observed orientations of terraces collected on the nucleus are unlikely to reflect an average topography, but they rather point to an internal structure which is now unevenly exposed on the comet.

This nucleus structure strongly suggests that the erosion of cometary material did not take place at the same rate, independently of the location on the body, but it has rather been not homogeneously distributed. In fact there are specific regions that experienced enhanced erosion, and others that still preserve the latest remnants of shallower terrains.

This concept is well illustrated in Fig. 6, where, for example, we can see that the Hathor region on the SL has been subject to an extended process of material removal, which produced a topographic surface cutting through the interior of the nucleus, confirming what already suggested by Thomas et al. (2015), Massironi et al. (2015) and Basilevsky et al. (2017).

Another not obvious conclusion of the analysis of our modelling is that we were able to clearly establish the pertinence of cometary material to either the BL or the SL. In fact, the geometry of the curved cliffs that can be observed on the shape model (see Fig. 12) in the Southern hemisphere, and the ridge in the Northern one (see Fig. 11) suggests a precise plane of junction between the two lobes.

Also, we observe that the Imhotep region on the BL is well aligned with one shell of the EM. This region is in fact predicted to be one of the deepest (in terms of layering) terrains that can be observed on the BL, thus suggesting it had experienced a process of material removal of more than 1 km of layers on its top.

Looking at Figs 6–9, not only is the original layered structure of each lobe evident, so providing confidence about their independent formation, but also that a significant portion of the layers in the proximity of the lobe junction is now lost (on top of the Hathor cliff). Since it is rather difficult to justify this missing material in terms of selective erosion driven by sublimation itself, it is very probable that this material was lost during the impact that led the two lobes to collide (Hirabayashi et al. 2016).

We have seen that the layers are defined by boundary discontinuity surfaces, which appear to be somehow more resistant to erosion. The geometry of these surfaces provides clearly an indication about the lateral continuity of the layers. Our model does not necessarily imply a global lateral persistence and/or a uniform thickness of the layers, but it demonstrates that the layers are aligned to an inner structure which does not follow the overall topography.

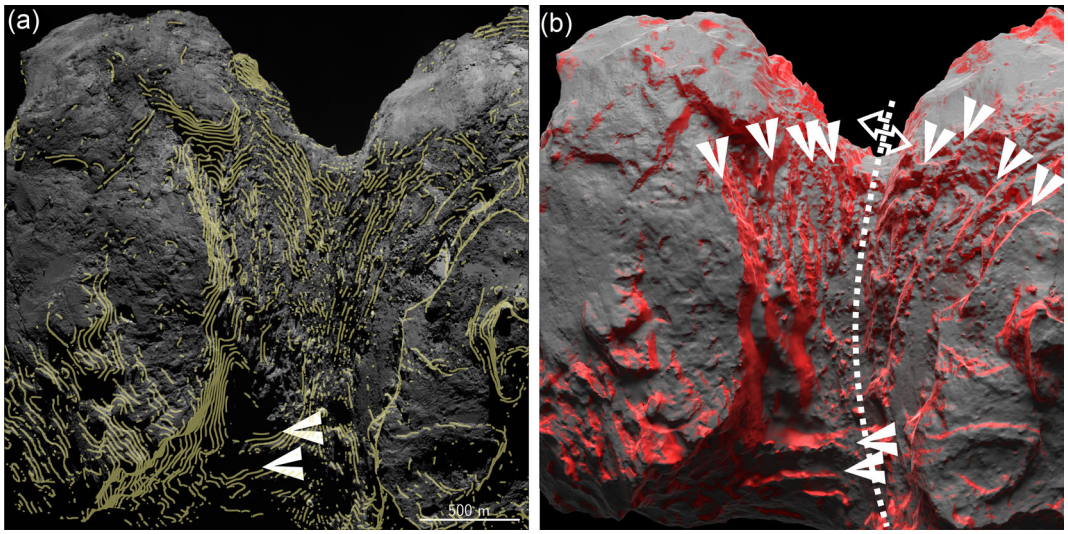

Figure 12. (a) OSIRIS image with the predicted layer orientation and (b) respective synthetic image of the shape model with slopes higher than 35° are shown in red (b). Arrows point along the direction of extended cliffs (red regions on the shape model), and especially on the BL (right lobe in (b) they exhibit a well-defined curved shape. Following the terraces on both the BL and SL a junction surface can be located and a possible separation line (dotted line) can be traced. The cliffs highlighted in the OSIRIS image well correspond to the contour lines of the model. ImageID reference: `NAC_2016-01-27T17.20.08.041`. For interpretation of the colours in this figure, the reader is referred to the web version of this article.

This idea is illustrated in Fig. 13: here the different conceptual models are purely based on the orientation of planar features (terraces) and does not necessarily require those surfaces to be of global extension. The proposed model in fact implies that the ellipsoidal shells are continuous inside the nucleus: this assumption must be considered a simplification required to obtain a model with a finite number of parameters. As an example, Fig. 13(a) shows *uniform* layers globally covering a lobe: this can be considered as the simplest but also perhaps less probable layering structure. Cases as shown in Fig. 13(b), where the discontinuity surfaces intersect, or in Fig. 13(c), where the surfaces are of limited extension, can be considered as well and would be coherent with the accretion models proposed by Belton et al. (2007) and Davidsson et al. (2016). Also configurations like the one represented in Fig. 13(d) are possible, in which the local density of the layer-defining discontinuities varies. However in all the cases, we have to remember both the long linear features observed on Hathor and Wosret (>0.5 km), and the large flat of the Imhotep region, which itself comprises an area >0.7 km^2 (Thomas et al. 2015). These extended features suggest that the scale of the layer surfaces can definitely be as large as several hundred metres, and probably more.

Finally, we can make some considerations about the accuracy of our model. To constrain the EMs, the local orientation of terraces has been used as a proxy for the local orientation of a corresponding layer discontinuity surface. These vectors have been computed on the latest available shape model for the comet, which has been obtained by OSIRIS images. The errors introduced by the best-fitting plane determination are expected to be around 5° (Massironi et al. 2015) and are probably much smaller than the errors introduced by the effect of erosion and fine material deposits on the terraces (see Fig. 3). This last error cannot be easily quantified, although regions with gravitational slopes in between 0 and 20° appear to be extensively covered by fine material (Groussin et al. 2015). Errors introduced by the dust cover could be expected to be in that range, as a simple approximation. Residuals for the MLE, show that the average accuracy of prediction for the terrace orientation is below 20°. Although this error might seem rather important it might be well

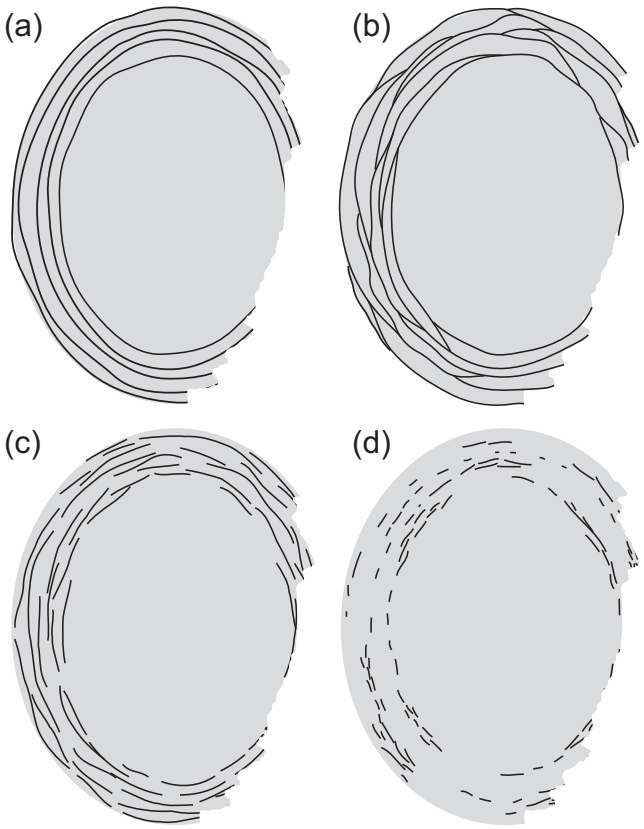

Figure 13. Conceptual models showing how various configurations of discontinuities can lead to stair-step-like organization of terraces. Surfaces might even have lateral variations causing layers to laterally change thickness or to be well defined only locally. The scale of this 'locality' of layers must still be greater than several hundreds of metres, given this is the scale of several laterally persistent cliffs and terraces that can be observed. The discontinuities in all these cases describe a global ordered structure, which is now unevenly exposed.

comparable with the errors introduced by erosion and deposition of taluses on the terraces. Furthermore, we have to consider that the ellipsoid-based model is definitely not the optimal model to represent the structure although it appears a fair assumption for a first, approximated analysis.

7 CONCLUSIONS

The morphological terraces observed on 67P have been previously connected with an inner layering (Massironi et al. 2015). Layers are defined by extended discontinuities, which form the flat surfaces of the terraces and cut the nucleus in correspondence of the linear traces observed on cliffs.

We have here shown that the observed flat surfaces, the linear traces and the laterally persistent cliffs can be explained by a simple ellipsoid-based model, which represents each layer-defining discontinuity surface as an ellipsoidal shell. The modelled discontinuities must be of local (at least several hundreds of metres) to possibly global extension (thousands of metres) to justify the extended cliffs and terraces.

The proposed three-dimensional model of the inner structure results to be misaligned with respect to the observed average topography, demonstrating the existence of an inner structure that is now unevenly exposed on the cometary surface.

This model has clearly the limitations of using ellipsoidal surfaces to fit the terraces and of keeping fixed the ellipsoids axis ratios. However, this must be considered a first order approximation of a more complex model which would be needed to better constrain the internal structure of the layer-defining discontinuities, and the relative layers thicknesses.

Even with this rough model we have been able to correlate actual features observed on the nucleus with the predicted internal structure of discontinuities. This confirms that the two lobes of 67P are characterized by a pervasive set of layer-defining discontinuities, roughly aligned with ellipsoidal shapes, and which do not follow the present surface.

Discussing the possible morphological phenomena which created the observed terraces and cliffs goes beyond the scope of this work, although our geometrical model now provides a solid support for the quantification of the involved processes.

The derived structure of the comet nucleus represents a geometric object that has evolved from the initial configuration in which the observed discontinuities were created to the complex object that was observed by OSIRIS, with a possible complicated history of highly localized removal of large volumes of material.

ACKNOWLEDGEMENTS

OSIRIS was built by a consortium of the Max-Planck-Institut für Sonnensystemforschung, in Göttingen, Germany, CISAS-University of Padova, Italy, the Laboratoire d'Astrophysique de Marseille, France, the Instituto de Astrofisica de Andalucia, CSIC, Granada, Spain, the Research and Scientific Support Department of the European Space Agency, Noordwijk, The Netherlands, the Instituto Nacional de Tecnica Aeroespacial, Madrid, Spain, the Universidad Politechnica de Madrid, Spain, the Department of Physics and Astronomy of Uppsala University, Sweden, and the Institut für Datentechnik und Kommunikationsnetze der Technischen Universität Braunschweig, Germany. The support of the national funding agencies of Germany (DLR), Italy (ASI), France (CNES), Spain (MEC), Sweden (SNSB), and the ESA Technical Directorate is gratefully acknowledged. We thank the ESA teams at ESAC, ESOC and ESTEC for their work in support of the Rosetta mission.

Authors thank Marco Franceschi, Andrea Bistacchi, and Sophie Viseur for the fruitful discussions about three-dimensional modelling of geological bodies. Snapshots of the shape model were produced with VTK/ParaView (www.paraview.org) and Blender (www.blender.org). Plots produced with matplotlib (www.matplotlib.org).

REFERENCES

Agarwal S., Mierle K., Others, 2016, Ceres Solver
Auger A.-T. et al., 2015, A&A, 583, A35
Basilevsky A., Mall U., Keller H., Skorov Y., Hviid S., Mottola S., Krasilnikov S., Dabrowski B., 2017, Planet. Space Sci., 137, 1
Belton M. J. et al., 2007, Icarus, 187, 332
Bruck Syal M., Schultz P. H., Sunshine J. M., A'Hearn M. F., Farnham T. L., Dearborn D. S., 2013, Icarus, 222, 610
Cheng A., Lisse C., A'Hearn M., 2013, Icarus, 222, 808
Chernick M. R., 2008, Bootstrap Methods: A Guide for Practitioners and Researchers, 2nd edn. Wiley Series in Probability and Statistics. Wiley-Interscience, Hoboken, N.J
Davidsson B. J. R. et al., 2016, A&A, 592, A63
Diebel J., 2006, Representing Attitude: Euler Angles, Unit Quaternions, and Rotation Vectors
Efron B., 1979, Ann. Stat., 7, 1
El-Maarry M. R. et al., 2015a, Geophys. Res. Lett., 42, 5170
El-Maarry M. R. et al., 2015b, A&A, 583, A26
El-Maarry M. R. et al., 2016, A&A, 593, A110
El-Maarry M. R. et al., 2017, A&A, 598, C2
Giacomini L. et al., 2016, MNRAS, 462, S352
Groussin O. et al., 2015, A&A, 583, A32
Hirabayashi M. et al., 2016, Nature, 534, 352
Jorda L. et al., 2016, Icarus, 277, 257
Jutzi M., Benz W., 2017, A&A, 597, A62
Jutzi M., Benz W., Toliou A., Morbidelli A., Brasser R., 2017, A&A, 597, A61
Keller H. U. et al., 2007, Space Sci. Rev., 128, 433
Lee J.-C. et al., 2017, MNRAS, 462, S573
Marchi S. et al., 2015, in Lunar and Planetary Science Conference. p. 1532
Massironi M. et al., 2015, Nature, 526, 402
Pajola M. et al., 2015, A&A, 583, A37
Pajola M. et al., 2016a, A&A, 592, L2
Pajola M. et al., 2016b, A&A, 592, A69
Pajola M. et al., 2017, Nat. Astron., 1, 0092
Preusker F. et al., 2017, A&A, 607, L1
Preusker F. et al., 2015, A&A, 583, A33
Rickman H. et al., 2015, A&A, 583, A44
Sierks H. et al., 2015, Science, 347, aaa1044
Thomas N. et al., 2015, Science, 347, aaa0440
Vincent J.-B. et al., 2015, Nature, 523, 63
Werner R., 1994, Celest. Mech. Dyn. Astron., 59, 253

SUPPORTING INFORMATION

Supplementary data are available at *MNRAS* online.

Please note: Oxford University Press is not responsible for the content or functionality of any supporting materials supplied by the authors. Any queries (other than missing material) should be directed to the corresponding author for the article.

[1] *Center of Studies and Activities for Space, CISAS, 'G. Colombo', University of Padova, Via Venezia 15, I-35131 Padova, Italy*
[2] *Geosciences Department, University of Padova, Via G. Gradenigo 6, I-35131 Padova, Italy*

[3]*Department of Physics and Astronomy, University of Padova, Via Marzolo 8, I-35131 Padova, Italy*
[4]*CNR-IFN UOS Padova LUXOR, Via Trasea 7, I-35131 Padova, Italy*
[5]*INAF – OAPD Astronomical Observatory of Padova, Vic. Osservatorio 5, I-35122 Padova, Italy*
[6]*NASA Ames Research Center, Moffett Field, CA 94035, USA*
[7]*German Aerospace Center (DLR), Institute of Planetary Research, D-12489 Berlin, Germany*
[8]*Aix Marseille Universite, CNRS LAM (Laboratoire d'Astrophysique de Marseille), UMR 7326, F-13388 Marseille, France*
[9]*Planetary Science Institute, 1700 East Fort Lowell, Suite 106, Tucson, AZ 85719, USA*
[10]*Department of Physics and Astronomy 'G. Galilei', University of Padova, Vic. Osservatorio 3, I-35122 Padova, Italy*
[11]*NASA Jet Propulsion Laboratory, 4800 Oak Grove Drive, Pasadena, CA 91109, USA*
[12]*Max-Planck-Institut für Sonnensystemforschung, Justus-von-Liebig-Weg 3, D-37077 Göttingen, Germany*
[13]*Laboratoire d'Astrophysique de Marseille, UMR 7326 CNRS & Aix-Marseille Université, 38 rue Frédéric Joliot-Curie, F-13388 Marseille cedex 13, France*
[14]*Centro de Astrobiologa, CSIC-INTA, E-28850 Torrejon de Ardoz, Madrid, Spain*
[15]*International Space Science Institute, Hallerstrasse 6, CH-3012 Bern, Switzerland*
[16]*Scientific Support Office, European Space Research and Technology Centre/ESA, Keplerlaan 1, Postbus 299, NL-2201 AZ Noordwijk ZH, the Netherlands*
[17]*Department of Physics and Astronomy, Uppsala University, SE-75120 Uppsala, Sweden*
[18]*PAS Space Research Center, Bartycka 18A, PL-00716 Warszawa, Poland*
[19]*Institute for Geophysics and Extraterrestrial Physics, TU Braunschweig, D-38106 Braunschweig, Germany*
[20]*Department for Astronomy, University of Maryland, College Park, MD 20742-2421, USA*
[21]*LESIA, Observatoire de Paris, PSL Research University, CNRS, Univ. Paris Diderot, Sorbonne Paris Cité, UPMC Univ. Paris 06, Sorbonne Universités, 5 place Jules Janssen, F-92195 Meudon, France*
[22]*LATMOS, CNRS/UVSQ/IPSL, 11 boulevard d'Alembert, F-78280 Guyancourt, France*
[23]*Department of Mechanical Engineering, University of Padova, Via Venezia 1, I-35131 Padova, Italy*
[24]*UNITN, University of Trento, Via Mesiano, 77, I-38100 Trento, Italy*
[25]*INAF – Osservatorio Astronomico, Via Tiepolo 11, I-34014 Trieste, Italy*
[26]*Instituto de Astrofisica de Andalucia CSIC, Glorieta de la Astronomia, E-18008 Granada, Spain*
[27]*Department of Earth Sciences, National Central University, 300 Chung-Da Rd, Chung-Li 32054, Taiwan*
[28]*Space Science Institute, Macau University of Science and Technology, Macau, China*
[29]*Operations Department, European Space Astronomy Centre/ESA, P.O. Box 78, E-28691 Villanueva de la Cañada, Madrid, Spain*
[30]*Physikalisches Institut der Universität Bern, Sidlerstr 5, CH-3012 Bern, Switzerland*

This paper has been typeset from a TEX/LATEX file prepared by the author.